OPEN ACCESS
Journal of Innovative Optical Health Sciences
Vol. 17, No. 3 (2024) 2350033 (11 pages)

DOI: 10.1142/S1793545823500335

World Scientific
www.worldscientific.com

Vein visualization enhancement by dual-wavelength phase-locked denoising technology

Lihua Ruan[*,§], Zhiqin Yin[*,†,‡,§], Shibing Zhou[*,§], Weibo Zheng[*,§,††], Wei Lu[*,†,‡,§,¶,‖], Tao Zhang[*,§,¶,**] and Shaowei Wang[*,†,‡,§,‡‡]

[*]*Shanghai Institute of Technical Physics, Chinese Academy of Sciences, Shanghai 200083, P. R. China*

[†]*State Key Laboratory of Infrared Physics, Shanghai Institute of Technical Physics, Chinese Academy of Sciences, Shanghai 200083, P. R. China*

[‡]*Shanghai Engineering Research Center of Energy-Saving Coatings Shanghai 200083, P. R. China*

[§]*University of Chinese Academy of Sciences, Beijing 100049, P. R. China*

[¶]*Shanghai Tech University, Shanghai 201210, P. R. China*

[‖]*School of Physical Science and Technology, ShanghaiTech University, Shanghai 201210, P. R. China*

[**]*School of Information Science and Technology, ShanghaiTech University, Shanghai 201210, China*

[††]*weibo_zheng@sina.com*

[‡‡]*wangshw@mail.sitp.ac.cn*

Received 9 September 2023
Revised 21 November 2023
Accepted 1 December 2023
Published 29 January 2024

Visual near-infrared imaging equipment has broad applications in various fields such as venipuncture, facial injections, and safety verification due to its noncontact, compact, and portable design. Currently, most studies utilize near-infrared single-wavelength for image acquisition of veins. However, many substances in the skin, including water, protein, and melanin can create significant background noise, which hinders accurate detection. In this paper, we developed a dual-wavelength imaging system with phase-locked denoising technology to acquire vein image. The signals in the effective region are compared by using the absorption valley and peak of hemoglobin at 700 nm and 940 nm, respectively. The phase-locked denoising algorithm is

[††,‡‡]Corresponding authors.

applied to decrease the noise and interference of complex surroundings from the images. The imaging results of the vein are successfully extracted in complex noise environment. It is demonstrated that the denoising effect on hand veins imaging can be improved with 57.3% by using our dual-wavelength phase-locked denoising technology. Consequently, this work proposes a novel approach for venous imaging with dual-wavelengths and phase-locked denoising algorithm to extract venous imaging results in complex noisy environment better.

Keywords: Dual-wavelength; phase-locked denoising; vein visualization enhancement.

1. Introduction

Venipuncture, a medical technique that involves inserting a needle into the wall of a vein to draw blood for analysis or drug administration, is a common procedure in modern medical treatment.[1,2] Despite the small incisions, venipuncture is still an invasive procedure that can cause pain and discomfort for the patient and even irreversible medical errors that threaten the patient's life.[3–6] Currently, the location for venipuncture is determined mainly by the experience of medical staff. However, some patients with thin or hard-to-find veins, such as children, obese individuals and darker-skinned patients, may experience difficulties during the procedure and cause additional suffering.[7–9] In biometric identification, finger veins and palm veins are more stable and reliable than fingerprint identification. These veins are located beneath the skin and are protected by it, which means external factors like superficial wounds, dirt, humidity and aging will not affect the results. Moreover, the flow of blood in living veins makes replication difficult and is safer than other biometric identification methods.[10–15]

At present, there are various devices available to help medical staff locate veins, but visualization is one of the most direct and effective methods.[16,17] Vein imaging works on the principle that hemoglobin in the vein has higher absorption in the near-infrared region, which results in the vein structure exhibiting stronger absorption than other surrounding tissues. This causes the color of vein to deepen and forms a light-dark contrast.[18] Medical research shows that near-infrared light with wavelength range of 700–1100 nm is capable of penetrating human skin and entering the subcutaneous tissue.[19] Hemoglobin in the blood is more sensitive to the 750 nm wavelength and has a larger absorption. For example, Lee *et al.*[20] and Juric *et al.*[16] both adopted 750 nm wavelength as the incident light source. However, the penetration depth of this wavelength is limited, and individuals with higher levels of body fat may require a light source with longer wavelength. Taking skin color into account, Shahzad *et al.* selected the near-infrared light source in the range of 750–950 nm to study the optimal illumination for vein imaging system.[9] Their results showed that the optimal illumination range is between 800 and 850 nm. Similarly, Kabaciński *et al.*,[21] Lee *et al.*,[22] and Zhao *et al.*[23] all used near-infrared light near 850 nm as the incident light source. Compared to the near-infrared light of 750 nm and 850 nm, the penetration depth of 940 nm to the skin is the largest, which avoids the peak of fat absorption coefficient. Therefore, Ma *et al.*[24] and Horng *et al.*[15] chose this band as the detection band. However, single-wavelength vein imaging cannot make full use of the optical properties of different biological tissues of the human body. Researchers have begun to explore the use of multi-band combined illumination or multispectral imaging to further enhance the contrast between subcutaneous veins and surrounding tissues. For example, Wang *et al.* utilized multispectral information in five bands to enhance the contrast and performance of vein detection.[25]

Near-infrared imaging equipment holds broad application prospects for vein imaging with its noncontact, small, and portable advantages.[17,26] This equipment mainly includes a light source, image acquisition device, and sensor. Two primary imaging modes are available: Transmission and reflection. The transmission mode requires a strong incident light source to penetrate the detection part, which places strict demands on the light source. As a result, most imaging equipment choose the reflection mode for measurement.[27,28] Currently, in vein image processing, techniques such as Gaussian filtering,[29,30] Gabor filtering,[20,24,31] and other methods are utilized to achieve excellent results in texture identification. For example, Ma *et al.* employed an adaptive two-dimensional Gabor filter to extract and

recognize palm veins, achieving remarkable performance with the equal error rate (EER) of 0.12%.[24] Similarly, Bharathi *et al.* used an improved two-dimensional Gabor filter to extract features of palm and finger vein images with an accuracy rate of 99.5%.[10] Additionally, deep learning neural networks have been applied in vein image processing. For example, Qin *et al.* demonstrated the strong accuracy and robustness of deep learning methods for vein images of varying quality through convolutional neural network (CNN) network prediction, segmentation, and extraction of vein networks.[32] Chen *et al.* is based on a lightweight CNN and an adaptive multispectral approach with interpretable artificial intelligence (AI) for vein image recognition, addressing the issues of data insufficiency and multispectral adaptability.[33] Although these methods have shown good results in texture discrimination, they may not be as effective in the restoration and extraction of small signals. Most substances in the skin, such as water, protein, and melanin cause a lot of background noise, which is not conducive to the test results. Furthermore, the penetration depth of near-infrared light sources is limited, and hemoglobin in the vein is difficult to detect in complex background environment, making it challenging to extract.

Therefore, this paper proposes a novel approach for venous imaging with dual-wavelengths and phase-locked denoising algorithm to extract venous imaging results in complex noisy environment.

2. Materials and Methods

2.1. *Selection of light source*

Different skin tissues have varying abilities to absorb near-infrared light, with longer wavelengths penetrating deeper into the skin layers containing veins and subcutaneous fat. In the near-infrared band, hemoglobin (including oxyhemoglobin and deoxygenated hemoglobin) and surrounding tissues in the veins have varying absorption capabilities. This allows reflected near-infrared light to carry information about subcutaneous blood vessels and can be distinguished from surrounding skin tissues. We measured the absorption spectrum of venous blood from the fingertip, as shown in Fig. 1. It can be seen that an absorption valley near 700 nm and an absorption peak near 940 nm promote the formation of signal contrast in the effective area. Therefore, the light sources of these two wavelengths are selected as the light sources for this work.

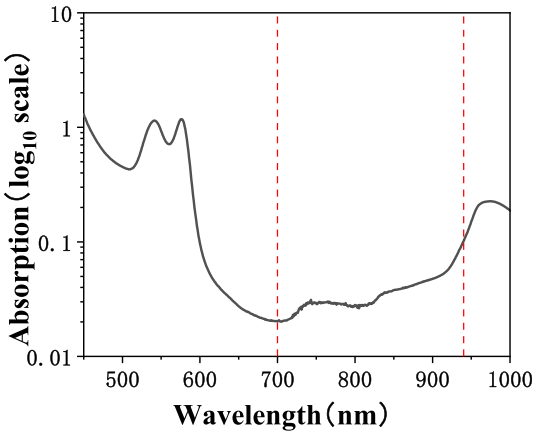

Fig. 1. The absorption spectrum of hemoglobin in the near-infrared band.

2.2. *Phase-locked denoising algorithm*

The phase-locked denoising algorithm follows the same principle as the lock-in amplifier. It utilizes the periodicity of signal and randomness of noise to extract the essential information such as the amplitude and phase of the original signal, through cross-correlation operations. This method aims to eliminate noise, restore the initial signal, and enhance the signal-to-noise ratio. The specific formula of the phase-locked denoising algorithm is derived as follows:

A signal submerged in noise can be expressed as follows:

$$X(t) = I(t) + \text{noise}(t), \tag{1}$$

where $X(t)$ is the original one that contains both the signal and the noise.
$I(t)$ represents the effective part of the signal.
noise(t) represents the noise.

Additionally, the signal can be regarded as the superposition of N sinusoidal signals:

$$I(t) = \sum_{i=1}^{N} A_i \sin(\omega_i t + \theta_i). \tag{2}$$

Here A_i, $f_i = \frac{\omega_i}{2\pi}$ and θ_i represent the amplitude, frequency, and phase of the ith frequency component, respectively.

To extract the signal from the noise, the signal to be processed is cross-correlated with a reference signal of a certain frequency. Since there is no correlation between the noise and the reference signal, the cross-correlation operation result is zero, and only the signal of the corresponding frequency is not zero.

Suppose that the reference signals of the kth frequency component $v_k(t)$ and $w_k(t)$ are basic cosine signal and sine signal:

$$\begin{cases} v_k(t) = \sin(\omega_k t), \\ w_k(t) = \cos(\omega_k t), \end{cases} \tag{3}$$

where ω_k is the angular velocity of the kth frequency component.

Cross-correlating the signal with the reference signal:

$$\begin{cases} R_{xv}(\tau) = E[X(t-\tau)v_k(t)], \\ R_{xw}(\tau) = E[X(t-\tau)w_k(t)], \end{cases} \tag{4}$$

where $R(\tau)$ represents a cross-correlation function that describes the degree of correlation between the values of two random signals at any two different moments, τ is the time lag of X signal against the reference signal and the E function represents the mathematical expectation of a random process.

Expanding the calculation of formula (4):

$$\begin{cases} R_{xv}(\tau) = \dfrac{A_k}{2}\cos(\theta_k - \omega_k\tau), \\ R_{xw}(\tau) = \dfrac{A_k}{2}\sin(\theta_k - \omega_k\tau). \end{cases} \tag{5}$$

When τ is 0, the amplitude and phase of the signal component at the kth frequency in $I(t)$ are obtained:

$$\theta_k = \tan^{-1}\frac{R_{xw}(0)}{R_{xv}(0)}, \tag{6}$$

$$A_k = 2\sqrt{R_{xv}^2(0) + R_{xw}^2(0)}. \tag{7}$$

The signal components of all frequencies are found first, then the effective part of the signal $I(t)$ is finally extracted from the original signal $X(t)$.

The efficacy of the two-dimensional phase-locked denoising algorithm on image is demonstrated through the leaf image. The original image of leaf is shown in Fig. 2(a), where the gray value of the

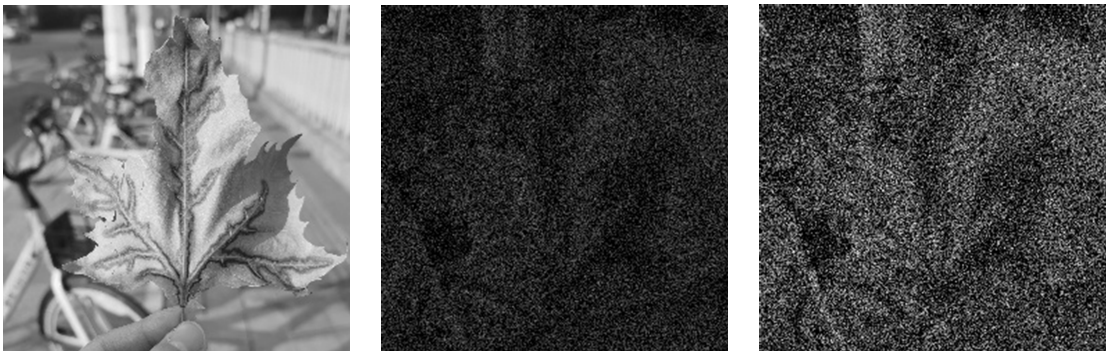

(a) (b) (c)

(d)

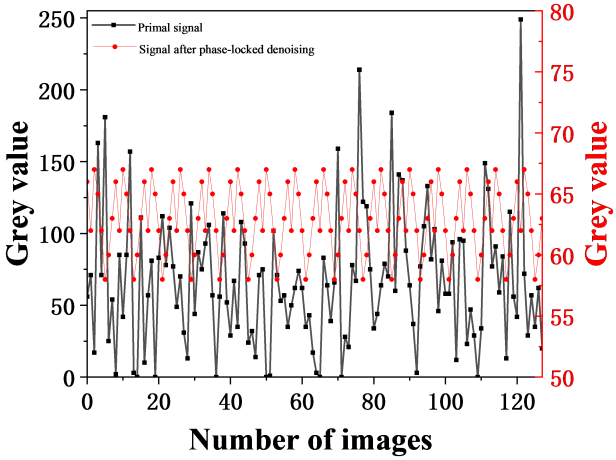

(e)

Fig. 2. (a) Original image of leaf. (b) and (c) Two groups of different gray value images after adding SNR = −10 dB Gaussian noise. (d) The image restored by the phase-locked denoising algorithm. (e) Comparison of signals at the same coordinate positions before and after phase-locking denoising.

position coordinate (i, j) of each pixel in the image is represented by $I(i, j)$.

Create a set of leaf image sequences with light and dark changes:

$$I\_\mathrm{low}(i,j) = \frac{I(i,j)}{255} \times 50, \tag{8}$$

$$I\_\mathrm{high}(i,j) = \frac{I(i,j)}{255} \times 100. \tag{9}$$

Gaussian noise with SNR $= -10$ dB is then added to each sequence, resulting in Figs. 2(b) and 2(c). (See Supplementary Material S1 for details on the addition of Gaussian noise.) These steps are repeated 64 times, generating 64 images of the two gray values, totaling 128 images. Images with the same gray value are grouped every four, and the gray values of pixels at the same coordinate position (157, 70) are extracted alternately to form a sequence, as shown by the black line in Fig. 2(e). The effective signals are submerged in complex background noise, making it difficult to distinguish. The image restored by the phase-locked denoising algorithm is shown in Fig. 2(d), and the signal is depicted by the red line in Fig. 2(e). It is evident that the noise interference has been significantly suppressed compared to before the phase-locked denoising, and the effective signal shows periodicity.

Peak signal-to-noise ratio (PSNR) is an objective standard for evaluating images, which is defined as the ratio of the square of the maximum value of the signal to the mean square error (MSE).

For a certain image I with a reference image I_ref, MSE is calculated as follows:

$$\mathrm{MSE} = \frac{1}{p \times q} \sum_{i=0}^{p-1} \sum_{j-0}^{q-1} [I(i,j) - I\_\mathrm{ref}(i,j)]^2, \tag{10}$$

where $(p,\ q)$ is the size of image I and I_ref $(i,\ j)$ represents the position of pixels.

PSNR is usually expressed in decibels, so the logarithm of the ratio is taken:

$$\mathrm{PSNR} = 10 \log \frac{\max_I^2}{\mathrm{MSE}}, \tag{11}$$

where $\max_I$ is the maximum of image I.

Structure Similarity Index Measure (SSIM) is an evaluation index used to evaluate the similarity of image luminance, contrast, and structure. For **I** and **I_ref**:

$$\mathbf{SSIM}(\mathbf{I}, \mathbf{I_{ref}}) = \frac{(2\boldsymbol{\mu}_\mathbf{I}\boldsymbol{\mu}_{\mathbf{I_{ref}}} + \mathbf{c_1})(2\boldsymbol{\sigma}_{\mathbf{II_{ref}}} + \mathbf{c_2})}{(\boldsymbol{\mu}_\mathbf{I}^2 + \boldsymbol{\mu}_{\mathbf{I_{ref}}}^2 + \mathbf{c_1})(\boldsymbol{\sigma}_\mathbf{I}^2 + \boldsymbol{\sigma}_{\mathbf{I_{ref}}}^2 + \mathbf{c_2})}, \tag{12}$$

$$\mathbf{c_1} = (\mathbf{0.01\,L})^2, \tag{13}$$

$$\mathbf{c_2} = (\mathbf{0.03\,L})^2, \tag{14}$$

where $\boldsymbol{\mu}_\mathbf{I}$ and $\boldsymbol{\sigma}_\mathbf{I}$ are the gray mean and variance of image **I**, respectively.

$\boldsymbol{\mu}_{\mathbf{I\_ref}}$ and $\boldsymbol{\sigma}_{\mathbf{I\_ref}}$ are the gray mean and variance of image **I_ref**, respectively.

$\boldsymbol{\sigma}_{\mathbf{II\_ref}}$ represents the covariance of **I** and **I_ref**.

$\mathbf{c_1}$ and $\mathbf{c_2}$ are constants increased to maintain stability.

L represents the dynamic range of pixel values.

PSNR and SSIM of all images are calculated. The PSNR values of Figs. 2(c) and 2(d) were 14.1 dB, and 29.7 dB, respectively, which is twice that before restoration. The SSIM values of Figs. 2(c) and 2(d) were 0.186 and 0.935, respectively. Table 1 shows the restored results of the phase-locked denoising algorithm under different noise levels, which fully demonstrates that the phase-locked denoising algorithm can restore effective signals in complex background noise and reduce noise interference. (See Supplementary Material S2 for details of restored pictures and signals.)

When compared to other denoising methods like BM3D,[34] DnCNN,[35] and DVDNet,[36] the proposed method maintains a relatively good performance. All algorithms used for comparison are highly cited. BM3D is a classical noise reduction algorithm currently extensively employed in cell phone imaging, DnCNN is a CNN-based noise reduction algorithm and DVDNet is designed for multi-frame image denoising. The images restored by different denoising algorithms are shown in Fig. 3 and Table 2. The

Table 1. The restored results of the phase-locked denoising algorithm under different noise levels.

		15 dB	10 dB	5 dB	−5 dB	−10 dB	−15 dB	−20 dB
PSNR (dB)	before	36.7	32.2	27.6	18.2	14.1	10.3	7.7
	restore	39.4	39.5	39.6	36.0	29.7	22.1	16.0
SSIM	before	0.981	0.947	0.859	0.399	0.186	0.073	0.028
	restore	0.996	0.995	0.995	0.980	0.935	0.811	0.591

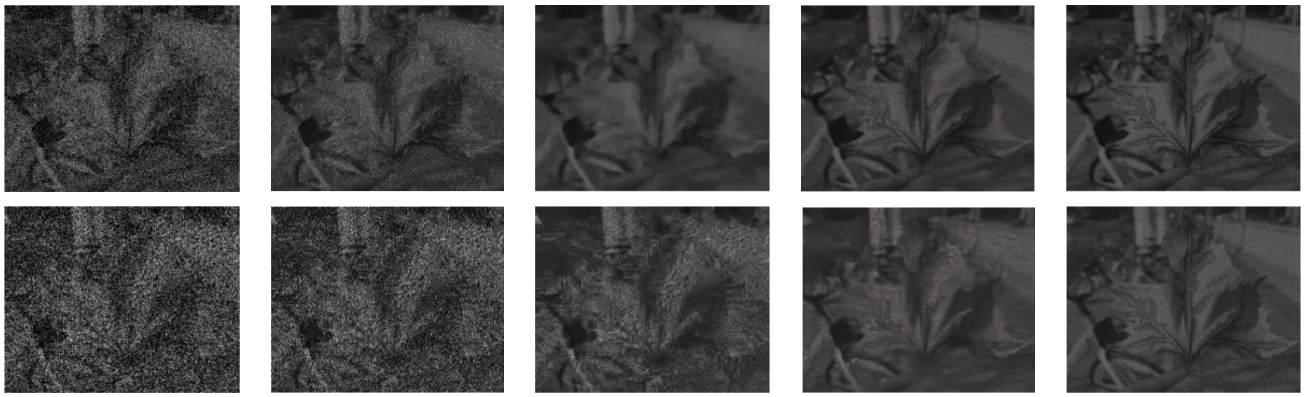

(a) Noisy (b) DnCNN (c) BM3D (d) DVDNet (e) ours

Fig. 3. (a) Noisy images after adding SNR = −5 dB (upper) and −10 dB (bottom) Gaussian noise. (b) The images restored by DnCNN from images in (a). (c) The images restored by BM3D from images in (a). (d) The images restored by DVDNet from images in (a). (e) The image restored by the proposed method from images in (a).

Table 2. The restored results of the different denoising algorithms under noise levels of −5 dB and −10 dB.

	−5 dB		−10 dB	
Methods	PSNR (dB)	SSIM	PSNR (dB)	SSIM
DnCNN	25.7	0.788	16.2	0.279
BM3D	31.0	0.925	22.5	0.631
DVDNet	33.4	0.956	28.8	0.904
ours	36.0	0.980	29.7	0.935

performance of these algorithms is respectable when the noise level is low. But when the noise is large, only DVDNet performs reasonably well, except for the proposed method.

3. Results

3.1. *Test system*

The imaging device we constructed in this paper employs reflective coaxial illumination, as illustrated in Figs. 4(a) and 4(c). The LED light source comprises two different wavelengths of 700 nm and 940 nm (Fig. 4(b)) which are the absorption valley and peak of hemoglobin, respectively. To ensure uniform illumination, two light sources are arranged in an alternating circle. The image acquisition device is placed in the annular hole at the center of LED light source. The object is placed directly underneath the light source to achieve coaxial illumination. The light source switching is controlled by a single-chip microcomputer for capturing images with the same acquisition time. Phase-locked denoising algorithm is

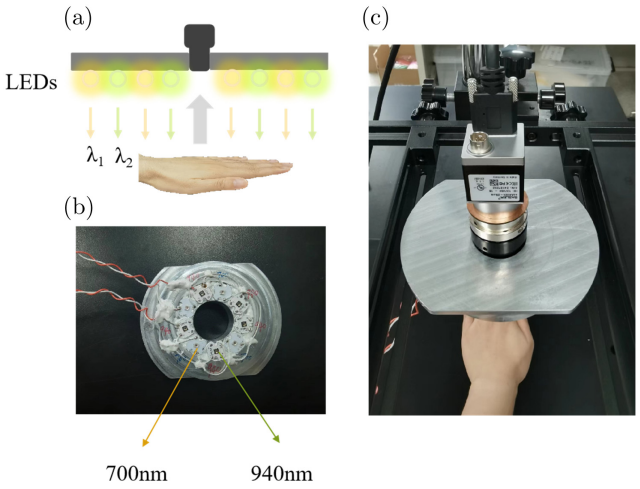

Fig. 4. (a) Schematic diagram of the imaging device, with reflective coaxial illumination. (b) The imaging light source adopts LEDs with two emission wavelengths of 700 nm and 940 nm, which are arranged alternately in a circle. (c) Prototype of the imaging device.

performed after capturing a series of imaging images at different wavelengths. The image is preprocessed using multi-angle Gabor fusion filtering, binarization, and other techniques. Clear vein contour texture information is obtained finally.

3.2. *Characterization*

The LEDs are purchased from Shenzhen Xinyi Optoelectronics Co., Ltd. The aluminum alloy substrate is used to dissipate heat for the LEDs. A silicon-based CMOS imaging detector (Sony IMX 226, Basler acA4024-29) is used as photodetector.

3.3. *Results of enhanced vein visualization*

Under the same shooting conditions, four images are taken for each wavelength by switching the light sources at a speed of 0.5 s. This process is repeated to obtain a series of images with time. See Supplementary Material S3 for all 128 images. The images are resized to reduce the calculation time by reducing the image size from 4024×3036 pixels to 216×162 pixels. The imaging results of the veins on the back of the experimenter's hand are presented in Fig. 5. Figures 5(b) and 5(c) are the imaging under the irradiation of two different light sources of 700 nm and 940 nm, respectively. It can be observed that the imaging effect is not obvious when using 700 nm light only, as it corresponds to the valley of hemoglobin absorption and is almost indistinguishable to naked eyes. Besides, the presence of body hair on the back of the hand is also a hindrance, especially for individuals with heavy body hair. In contrast, it reveals some veins on the back of the hand as shown in Fig. 5(c) when using 940 nm in the near-infrared band, which corresponds to the absorption peak of hemoglobin. However, it will produce white spots when the light source is too close to hand due to specific reflection angle and uneven surface of the hand, which will cause significant noise interference in subsequent processing steps such as filtering and binarization. The phase-locked denoising algorithm is applied to address this, and the resulting image is presented in Fig. 5(d). The veins on the back of the hand are clearly visible, and the reflection and body hair imaging are well suppressed after the treatment.

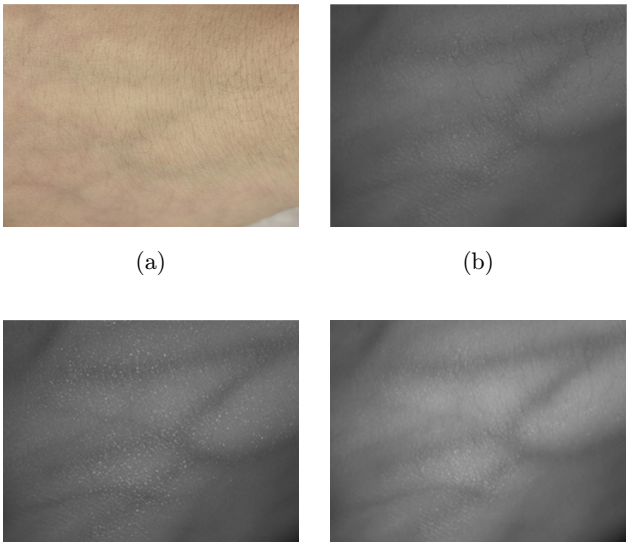

(a) (b) (c) (d)

Fig. 5. The image of back of the hand veins illuminated by (a) natural light, (b) 700 nm, and (c) 940 nm, respectively. The image of back of the hand veins after (d) phase-locked denoising.

A time-varying sequence is generated by extracting the gray value of each pixel in the same position. However, noise is introduced during the shooting process, such as stray light in the environment, dark current noise, and changes in the physical condition of the subject. The resultant complex background noise can obscure the effective signal and make it difficult to recover. Therefore, image preprocessing is necessary. To calculate the image sequence of the hand vein, a set of discrete square wave signals with known periods must be extracted. The sequence of pixel values at pixel point (i, j) can be expressed as follows:

$$X_{(i,j)}[n] = I_{(i,j)}[n] + \text{noise}_{(i,j)}[n], \quad n \in [0, N-1], \tag{15}$$

where N is the length of the image sequence and n represents the nth image.

According to the discrete Fourier transform, the discrete periodic square wave signal $I_{(i,j)}[n]$ to be restored can be expressed as follows:

$$\begin{aligned} I_{(i,j)}[n] = & \sum_{m=0}^{N_0-1} \left[A_k \left[m \frac{N}{N_0} \right] - \text{mean}(A_k) \right] \sin \\ & \times \left(\frac{2\pi * m}{N_0} n + \theta_k \left[m * \frac{N}{N_0} \right] \right), \\ & (n, k \in [0, N-1]), \end{aligned} \tag{16}$$

where N_0 is the number of sampling points in a period, which is the number of images in a period. mean is the function to find the mathematical mean.

The reference signal and cross-correlation are calculated as follows:

$$\begin{cases} v_k[n] = \sin\left(\dfrac{2\pi nk}{N}\right), \\ w_k[n] = \cos\left(\dfrac{2\pi nk}{N}\right), \end{cases} \tag{17}$$

$$\begin{cases} R_{xvk} = \dfrac{1}{N}\displaystyle\sum_{n=0}^{N-1} X[n]v_k[n], \\ R_{xwk} = \dfrac{1}{N}\displaystyle\sum_{n=0}^{N-1} X[n]w_k[n]. \end{cases} \tag{18}$$

The discrete A_k and θ_k can be calculated by combining formulas (6) and (7). This allows the signal sequence $I_{(i,j)}[n]$ at pixel point (i, j) to be obtained, and the pixel value $\tilde{I}(i, j)$ at the point is the average amplitude of the sequence:

$$\tilde{I}(i,j) = 2\sqrt{\frac{\sum_{k=0}^{N-1} A_k^2}{N}}. \tag{19}$$

Figure 6 shows the original signals of the skin and veins represented by the black and green dotted lines, respectively. It can be observed that their effective signals are completely submerged in the noise. The effects of the skin and veins after the phase-locked denoising algorithm are presented in Fig. 6, where the blue and purple solid lines indicate significant suppression of noise interference. It reveals that the periodicity of the effective signal, compared to the pre-phase-locking and denoising state.

To further demonstrate the effectiveness of phase-locked denoising technology, the images processed by the algorithm and those taken by the 940 nm light source were subjected to Gabor filtering and binarization, as shown in Fig. 7. Figures 7(a)–7(d) present the results of Gabor filtering and binarization for images with and without phase-locked denoising. The parameters of Gabor and the threshold of binarization are consistent in both images. It is evident that the vein signal of binarized image in Fig. 7(b) is significantly interfered by background noise with the areas marked by red dotted lines identified as veins by mistake. Figure 7(d) shows the image after phase-locked denoising process. It is much better than that of Fig. 7(b) thanks to the reduction of wrong information by our phase-locked denoising algorithm. The variance can be used for no-reference image quality evaluation.[37] The larger variance indicates a richer gray level and more information in the image. It is convenient to identify and classify substances, and the image quality is more ideal. Variance is the average value of the square of the difference between each sample data and the mean:

$$\mathrm{Var} = \frac{1}{p * q}\sum_{i=0}^{p-1}\sum_{j=0}^{q-1}(I(i,j) - \mathrm{mean}(I))^2, \tag{20}$$

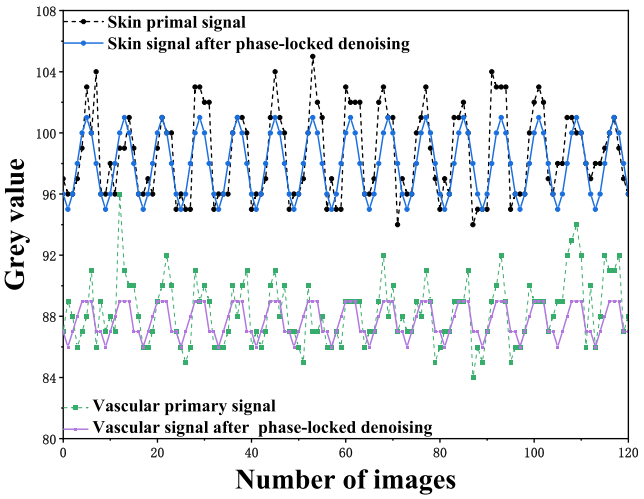

Fig. 6. Comparison of the original signal of skin and veins with the signal after phase-locked denoising process. The black dotted and blue solid lines represent the original skin signal and restored signal of the skin after phase-locked denoising process, respectively. The green dotted and purple solid lines represent the original signal and restored signal of the veins after phase-locked denoising process, respectively.

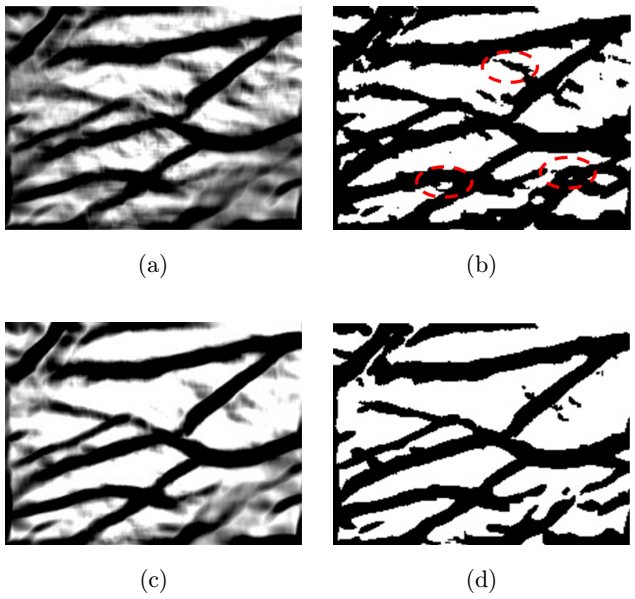

Fig. 7. Comparison of post-processing with and without phase-lock denoising algorithm. The image of back of the hand veins after illuminated by 940 nm light source is processed by (a) multi-angle Gabor fusion filter processing and (b) binarization, respectively. The areas marked by red dotted lines are identified as veins by mistake in Fig. 7(b). The image of back of the hand veins after phase-locked denoising is processed by (c) multi-angle Gabor filtering processing and (d) binarization, respectively.

where (p, q) is the size of the image and mean(I) is the average value of image I.

After calculating the 700 nm, 940 nm, and phase-locked denoising algorithm, the variance of the image is found to be 164.8, 225.6, and 354.9, respectively, resulting in 115.4% and 57.3% improvement in image quality of 700 nm and 940 nm, respectively.

4. Discussion

The noise reduction performance of a phase-locked denoising algorithm on multi-frame images has been investigated and then vascular visualization imaging in conjunction with a light source modulation approach was applied. Compared with currently used noise reduction algorithms, the algorithm shows significant performance advantages and has improved the quality of vascular imaging.

There are still some limitations to the algorithm. One of the limitations is that it has restrictions on the form of the acquired image, which needs to be modulated during the imaging phase. Another one is that the algorithm operates on a time series of images, which may cause some loss of efficiency. This kind of loss can probably be compensated for by utilizing the parallel computing power of chips such as FPGA while integrating the imaging device subsequently.

Despite these limitations, the effectiveness of the phase-locked denoising algorithm demonstrated in vascular imaging still hints at its potential for application in other imaging devices. We welcome other researchers to use this denoising algorithm and expand it to more application scenarios.

5. Conclusion

In conclusion, a phase-locked denoising technology has been developed to acquire vein image by using a dual-wavelength imaging system with absorption valley and peak of hemoglobin at 700 nm and 940 nm, respectively. The phase-locked denoising algorithm is applied to remarkably reduce the noise of complex surrounding and obtain the image of vein clearly. The results show that the denoising effect has been improved by at least 57.3% with dual-wavelength phase-locked denoising technology. Such a technology may be applied to recognize blood vessels in the facial periocular and other regions in future, where with higher fat content and deeper or relatively slender, which is more difficult to be identified.

Acknowledgments

This work was funded by National Key R&D Program of China (2021YFC2103300), National Key R&D Program of China (2021YFA0715500), National Natural Science Foundation of China (NSFC) (12227901), Strategic Priority Research Program (B) of the Chinese Academy of Sciences (XDB0580000) and Chinese Academy of Sciences President's International Fellowship Initiative (2021PT0007).

Conflict of Interest

We declare that we have no conflict of interest.

Data Statement

Data underlying the results presented in this paper were collected through experiments. Both code and data can be obtained from the authors upon reasonable request.

ORCID

Shaowei Wang https://orcid.org/0000-0002-6624-2016

References

1. D. Giavarina, G. Lippi, "Blood venous sample collection: Recommendations overview and a checklist to improve quality," *Clin. Biochem.* **50**(10–11), 568–573 (2017).
2. G. C. Meng *et al.*, Prototype design or wearable veins localization system using near infrared imaging technique, *IEEE 11th Int. Colloquium on Signal Processing & its Applications (CSPA)*, 6–8 March 2015, Kuala Lumpur, Malaysia, pp. 112–115.
3. T. A. Hotta, "Understanding the anatomy of the upper face when providing aesthetic injection treatments," *Plast. Surg. Nurs.* **36**(3), 104–109 (2016).
4. K. Nettar, C. Maas, "Facial filler and neurotoxin complications," *Facial Plast. Surg.* **28**(3), 288–293 (2012).
5. S. S. E. Park, A. Barmettler, "Vision loss secondary to facial and periorbital steroid injection: A

systematic review," *Ophthalmic Plast. Reconstr. Surg.* **37**(6), 511–521 (2021).
6. H. Qian *et al.*, "Massive cerebral infarction following facial injection of autologous fat: A case report and review of the literature," *Front. Human Neurosci.* **15**, 610945 (2021).
7. C. T. Pan *et al.*, "Vein pattern locating technology for cannulation: a review of the low-cost vein finder prototypes utilizing near infrared (NIR) light to improve peripheral subcutaneous vein selection for phlebotomy," *Sensors* **19**(16), 3573 (2019).
8. C. lalongo, S. Bernardini, "Phlebotomy, a bridge between laboratory and patient," *Biochem. Med.* **26**(1), 17–33 (2016).
9. A. Shahzad *et al.*, "Hyperspectral venous image quality assessment for optimum illumination range selection based on skin tone characteristics," *Biomedi. Eng. Online* **13**, 109 (2014).
10. S. Bharathi, R. Sudhakar, "Biometric recognition using finger and palm vein images," *Soft Comput.* **23**(6), 1843–1855. (2019).
11. W. G. Dong *et al.*, Research on multi-spectral adaptive method for palm vein capturing based on image quality, *32nd Youth Academic Annual Conf. Chinese Association of Automation (YAC)*, 19–21 May 2017, Hefei, China, pp. 1154–1157.
12. A. P. Savitha, Ramegowda, A comparative study of palm vein feature extraction and classification, *Int. Conf. Nanotechnology (ICNano).* (2016).
13. A. Alzubaidi, J. Kalita, "Authentication of Smartphone Users Using Behavioral Biometrics," *IEEE Commun. Surv. Tutor.* **18**(3), 1998–2026 (2016).
14. Y. F. Wang *et al.*, "V-Vibe: A robust ROI extraction method based on background subtraction for vein images collected by infrared device," *Infrared Physi. Technol.* **123**, 104175 (2022).
15. S. J. Horng *et al.*, "Recognizing palm vein in smartphones using RGB images," *IEEE Trans. Ind. Inf.* **18**(9), 5992–6002 (2022).
16. S. Juric *et al.*, "Towards a low-cost mobile subcutaneous vein detection solution using near-infrared spectroscopy," *Sci. World J.* **2014**, 365902 (2014).
17. J. Y. Pan *et al.*, "A miniaturized fluorescence imaging device for rapid early skin cancer detection," *J. Innov. Opt. Health Sci.* **14**(2), 2050026 (2021).
18. F. Scholkmann *et al.*, "A review on continuous wave functional near-infrared spectroscopy and imaging instrumentation and methodology," *Neuroimage* **85**, 6–27 (2014).
19. Y. B. Zhou, A. Kumar, "Human identification using palm-vein images," *IEEE Trans. Inf. Forensics Secur.* **6**(4), 1259–1274 (2011).
20. J. C. Lee *et al.*, "Dorsal hand vein recognition based on 2D Gabor filters," *Imag. Sci. J.* **62**(3), 127–138 (2014).
21. R. Kabacinski, M. Kowalski, "Vein pattern database and benchmark results," *Electron. Lett.* **47**(20), 1127–1128 (2011).
22. E. C. Lee, K. R. Park, "Image restoration of skin scattering and optical blurring for finger vein recognition," *Opt. Lasers Eng.* **49**(7), 816–828 (2011).
23. Q. Zhao *et al.*, Design and implementation of a contactless multiple hand feature acquisition system, *Conf. Sensing Technologies for Global Health, Military Medicine, Disaster Response and Environmental Monitoring II – and Biometric Technology for Human Identification IX.* 4 May 2012, Baltimore, Maryland, United States.
24. X. Ma *et al.*, "Palm vein recognition scheme based on an adaptive Gabor filter," *IET Biom.* **6**(5), 325–333 (2017).
25. F. Wang *et al.*, "High-contrast subcutaneous vein detection and localization using multispectral imaging," *J. Biomed. Opt.* **18**(5), 050504 (2013).
26. Z. Xuan *et al.*, "Artificial structural colors and applications," *Innov. J.* **2**(1), 159–173 (2021).
27. W. Wu *et al.*, "Review of palm vein recognition," *IET Biom.* **9**(1), 1–10 (2019).
28. M. Walus, K. Bernacki, J. Konopacki, "Impact of NIR wavelength lighting in image acquisition on finger vein biometric system effectiveness," *Opto-Electron. Rev.* **25**(4), 263–268 (2017).
29. A. Kirimtat, O. Krejcar, Parametric variations of anisotropic diffusion and gaussian high-pass filter for nir image preprocessing in vein identification, *Bioinformatics and Biomedical Engineering*, Lect. Notes Comput. Sci., Vol. 10814, pp. 212–220, Springer, Cham (2018).
30. A. M. Al-Juboori *et al.*, Biometric authentication system based on palm vein, *Int. Conf. Computer Sciences and Applications (CSA)*, 14–15 December 2013, Wuhan, China, pp. 52–58.
31. W.-Y. Han, J.-C. Lee, "Palm vein recognition using adaptive Gabor filter," *Expert Syst. Appl.* **39**(18), 13225–13234 (2012).
32. H. F. Qin, M. A. El-Yacoubi, "Deep representation-based feature extraction and recovering for finger-vein verification," *IEEE Trans. Inf. Forensics Secur.* **12**(8), 1816–1829 (2017).
33. Y. Y. Chen *et al.*, "Explainable AI: A multispectral palm-vein identification system with new augmentation features," *ACM Trans. Multimedia Comput. Commun. Appl.* **17**(3), 111 (2021).
34. K. Dabov *et al.*, "Image denoising by sparse 3-D transform-domain collaborative filtering," *IEEE Trans. Image Process.* **16**(8), 2080–2095 (2007).
35. K. Zhang *et al.*, "Beyond a Gaussian denoiser: Residual learning of deep CNN for image

denoising," *IEEE Trans. Image Process.* **26**(7), 3142–3155 (2017).

36. M. Tassano, J. Delon, T. Veit, DVDNET: A fast network for deep video denoising, *IEEE Int. Conf. Image Processing*, pp. 1805–1809, IEEE (2019).
37. J. P. Woodard, M. P. Carley-Spencer, "No-reference image quality metrics for structural MRI," *Neuroinformatics* **4**(3), 243–262 (2006).